Evaluation of stratospheric ozone, temperature, and aerosol profiles from the LOANA lidar in Antarctica

Christine David, Alexander Haefele, Philippe Keckhut, Marion Marchand, Julien Jumelet, Thierry Leblanc, Claire Cénac, Christian Laqui, Jacques Porteneuve, M. Haeffelin, et al.

Available online at www.sciencedirect.com

SciVerse ScienceDirect

Polar Science 6 (2012) 209–225

http://ees.elsevier.com/polar/

Evaluation of stratospheric ozone, temperature, and aerosol profiles from the LOANA lidar in Antarctica

C. David [a,f], A. Haefele [a,g,*], P. Keckhut [a], M. Marchand [a], J. Jumelet [a], T. Leblanc [b], C. Cenac [a,c], C. Laqui [a], J. Porteneuve [a], M. Haeffelin [c], Y. Courcoux [d], M. Snels [e], M. Viterbini [e], M. Quatrevalet [h]

[a] *LATMOS–IPSL, Université de Versailles Saint-Quentin, 78280 Guyancourt, France*
[b] *California Institute of Technology, Jet Propulsion Laboratory, Table Mountain Facility, Wrightwood, CA 92397-0367, USA*
[c] *Laboratoire de Météorologique Dynamique/IPSL, Ecole Polytechnique, 91128 Palaiseau, France*
[d] *Observatoire de Physique de l'Atmosphère de La Réunion, CNRS, 97715 Saint Denis, France*
[e] *ISAC–CNR, 00133 Rome, Italy*
[f] *Institut Polaire Français Paul Emile Victor, Technopôle Brest-Iroise, 29280 Plouzané, France*
[g] *MeteoSwiss, Chemin de l'Aérologie, 1530 Payerne, Switzerland*
[h] *Deutsches Zentrum für Luft- und Raumfahrt, Institut für Physik der Atmosphäre, Oberpfaffenhofen, Germany*

Received 5 December 2011; revised 11 June 2012; accepted 18 July 2012
Available online 27 July 2012

Abstract

We present an evaluation of observations from the Lidar Ozone and Aerosol for NDACC in Antarctica (LOANA) at the Dumont d'Urville station, Antarctica. This instrument is part of the Network for the Detection of Atmospheric Composition Change (NDACC), and ensures continuity with lidar measurements made since 1989 with the previous instrument at this site. This study is based on the dataset from 2008 to 2009, and comparisons are made with observations from balloon soundings, and from three satellite experiments: Aura/MLS, TIMED/SABER, and CALIOP/CALIPSO. The lidar ozone data are in very good agreement with the balloon sounding data (ECC sensor), revealing a bias of less than 3% between 17 and 34 km. For temperature, the lidar shows a low bias of −3 K at 20 km when compared with Aura/MLS. Between 30 and 50 km, the bias is less than 2 K. We also present our initial results showing diurnal variations in temperature. The amplitude of these diurnal cycles is on the order of 1 K and is unlikely to account for the temperature biases between LOANA and the reference instruments. Comparisons of total attenuated backscatter reveal good qualitative agreement between LOANA and CALIOP, with differences of less than 30% in the derived optical depth.

Keywords: Polar ozone; Polar stratospheric clouds; Lidar; Stratosphere

1. Introduction

Since the discovery of the Antarctic ozone hole in the 1980s, the stratosphere has been closely monitored to track its development, with the main focus being on the ozone layer itself. The Network for the Detection

* Corresponding author. MeteoSwiss, Chemin de l'Aérologie, 1530 Payerne, Switzerland.
E-mail address: alexander.haefele@meteoswiss.ch (A. Haefele).

1873-9652/$ - see front matter © 2012 Elsevier B.V. and NIPR. All rights reserved.
http://dx.doi.org/10.1016/j.polar.2012.07.001

of Atmospheric Composition Change (NDACC) was developed to carry out this monitoring work and it comprises about 70 high-quality remote sensing research stations that provide sophisticated measurements of major stratospheric species and parameters. Lidars constitute the main NDACC instrumentation, as they are well suited to the monitoring of ozone, temperature, aerosols, and polar stratospheric clouds (PSCs), which are all key elements in stratospheric ozone chemistry.

The French Antarctic station Dumont d'Urville (DDU, 66°40′S, 140°01′E), operated by the French Polar Institute (IPEV), and the US McMurdo station (77°51′S, 166°40′E), operated by US National Science Foundation (NSF), are NDACC Antarctic Primary sites. The first lidar instrument was installed at DDU within the framework of the Polar Ozone Lidar Experiment (POLE), a French–Italian collaboration between the Service dAronomie-IPSL and the IROE-CNR. POLE initiated a program of continuous monitoring of the stratosphere in the Antarctic region, following Montreal Protocol recommendations. The backscatter lidar used for aerosols and PSC measurements was set up in December 1988, and started operation in April 1989 (Sacco et al., 1989). This system was upgraded in January 1991 with a differential absorption lidar (DIAL) for ozone lidar, and was then able to sequentially measure the vertical distributions of both stratospheric ozone and stratospheric aerosols and PSCs (Stefanutti et al., 1992).

After more than a decade of use, the instrument became outdated and subject to an increasing number of failures, leading to outages in the ozone measurements and poor quality aerosols/PSC data. Consequently, the entire lidar system was redesigned in 2002, but without any significant changes to the layout of the instrument. This new Lidar for Ozone and Aerosols for NDACC in Antarctica (LOANA) was the result of a collaboration between LATMOS-IPSL (Laboratoire Atmosphère, Milieux, Observations Spatiales – Institut Pierre Simon Laplace, formerly SA-CNRS) and ISAC-CNR (Instituto di Scienze dell'Atmosfera e del Clima – Consiglio Nazionale delle Ricerche), and, like its predecessor, makes aerosol and PSC observations (from 8 to 32 km), and ozone measurements using the Raman detection technique (from 15 to 50 km). In addition, temperature profiles are now available from 20 to 65 km. LOANA was implemented at DDU in January 2005. Aerosols, PSCs, and temperature profiles are made simultaneously and have been available since 2006. Ozone measurements are performed sequentially and have been operational since 2008.

Except for 2000 (laser failure) and 2005 (test phase), aerosols and PSC measurements have been carried out at DDU every year since 1989, from roughly mid-February to the beginning of November (David et al., 1998, 2005; Santacesaria et al., 2001), providing the only continuous aerosol lidar time series from Antarctica that covers a period of 20 years. The aerosol/PSC lidar at McMurdo has been operational since 1991 (Adriani et al., 2004).

In this paper we present an evaluation of the ozone, temperature, and aerosol/PSC profiles obtained in 2008 and 2009 with the new LOANA lidar system. The Raman channels are not considered here, as they were still under testing and not operational at the time of writing. The paper is organized as follows. A description of the instrument is given in Section 2, followed by a discussion of the collation and processing of the raw data and retrieval of the geophysical parameters in Section 3. In Section 4, we present a validation of the ozone, temperature, and aerosol/PSC data, together with a first analysis of the diurnal variations in temperature, which are investigated using signals at a wavelength of 532 nm. A discussion of the results is given in Section 5.

2. Instrument description

LOANA was designed to operate in two distinct modes: one for ozone and temperature measurements (the ozone mode), and one for aerosol/PSC and temperature measurements (the aerosol mode). The ozone mode includes light emission and reception at wavelengths of 308 and 355 nm, and additional reception at 332 and 387 nm (ozone Raman channels). The aerosol mode includes emission and reception at wavelengths of 532 and 1064 nm, and additional reception at 608 nm (aerosol Raman channels). To emit at the required wavelengths, two different laser sources are used: an Nd:YAG laser (Quantel CFR400) that emits 500 mJ per pulse at 1064 nm with a repetition rate of 10 Hz, and which can be frequency doubled to emit 270 mJ per pulse at 532 nm, or frequency tripled to emit 55 mJ per pulse at 355 nm, and an excimer laser (GSI Lumonics Pulse Master PM848) that emits 200 mJ per pulse at 308 nm with a repetition rate of 80 Hz. Only the Nd:YAG is used in aerosol mode, while in ozone mode the Nd:YAG is associated with the excimer laser. A 3D schematic view of the lidar setup is shown in Fig. 1. The UV light from the excimer laser is directed vertically into the free atmosphere using a mirror with a 45° inclination, while the light from the Nd:YAG laser first passes through

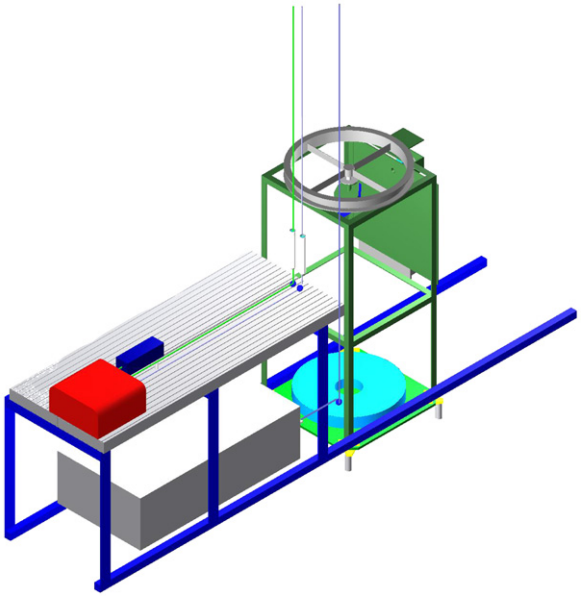

Fig. 1. The LOANA instrument setup within the lidar at DDU. The blue unit is the Nd:YAG laser, the red unit hosts the harmonic generators, and the gray unit at the bottom is the excimer laser.

a focal beam expander placed before the 45° mirror to reduce the divergence of the beam, which is around 0.03 mrad for both beams. Two optical fibers, located behind the mirrors, collect part of the emitted signals to register the time of departure of the signal, T_0, which is used to trigger the acquisition chain.

The backscattered signals are collected with a Newton telescope that has a diameter of 80 cm, and pass a mechanical chopper wheel, mounted at the focal point of the telescope, to minimize signal induced noise due to the intense signal returns from the lower altitudes. The lasers are synchronized using the chopper wheel aperture time. Dichroic mirrors are used to direct visible and IR wavelengths to the aerosol spectrometer unit, and UV wavelengths to the ozone spectrometer unit.

A schematic of the aerosol spectrometer unit is shown in Fig. 2 (left). A first dichroic beamsplitter, inclined at 45° with respect to the incident beam, directs the 532 nm signal onto a polarizing cube that splits the beam into two components polarized parallel and perpendicular to the laser emission. Both components are then detected by a photomultiplier. The parallel polarized beam is further separated by a coated glass window/beamsplitter into fractions of 98.3 and 1.7%, corresponding to the high- and low-altitude range channels respectively, which are again detected by photomultipliers. The signals at 608 and 1064 nm transmitted by the first beamsplitter are separated by a second beamsplitter, and detected by a photomultiplier and an avalanche photo diode, respectively.

The ozone spectrometer, also shown in Fig. 2 (right), includes a grating to separate the four wavelengths of 305, 355, 332, and 387 nm. A spherical mirror directs the Raman signals directly to the corresponding photomultipliers, while the Rayleigh signals are split into the high- and low-altitude range channels by a 90% versus 10% transmitting 45° inclination coated glass beamsplitter.

The photomultipliers used are all of the Hamamatsu R2693P type. The electronic signals from the photomultipliers are further amplified, and then recorded by four acquisition cards (Embedded Devices APC-80250DSP), each having two acquisition channels. All signals are time resolved with a sampling interval of 400 ns and a total of 2048 bins reaching an altitude of 120 km with a vertical resolution of 60 m. The signals are averaged over 3000 shots for the Nd:YAG wavelengths (1064, 532, and 355 nm), and over 24,000 shots for the excimer wavelengths (308 nm), corresponding to an averaging interval of 5 min, before being stored to disk.

3. Retrieval of geophysical parameters

3.1. Correcting the raw data

Before being inverted, the integrated signals are corrected for saturation at lower altitudes, typically below 20 km in ozone mode and below 5 km in aerosol mode, and the background signal is subtracted. For temperature retrieval, the signals are also corrected for Rayleigh extinction, ozone absorption, and range.

3.1.1. Background correction

The lidar signals are superimposed by random fluctuations (e.g., electronic noise), and also by background noise caused by natural stray light or light generated within the system. The background noise is not strictly constant with altitude, but can show a slight altitude dependence. Removal of the background signal is especially important at higher altitudes, where retrieval of geographical parameters is severely hindered. The signal to noise ratio (SNR) is used to determine the key altitudes for signal processing. The signal is calculated based on climatological profiles of pressure, temperature, and ozone, and then scaled to match the measured signal at a given altitude of 35, 40, 25, and 25 km for channels 308H, 355H, 308M, and 355M, respectively. The background noise is taken to be the mean value of the measured raw signal between 120 and 122 km.

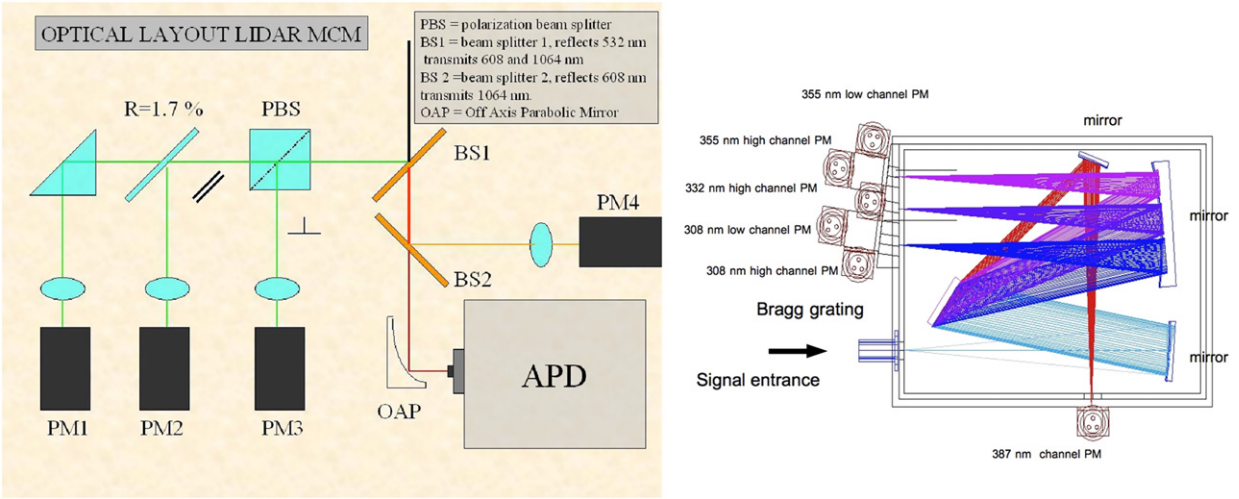

Fig. 2. Schematics of the spectrometer units in aerosol mode (left) and ozone mode (right). For details see text Section 2.

The SNR decreases with altitude, and an SNR of less than 0.01 indicates that the signal is dominated by the background noise and that the backscattered signal is negligible. A first or second order polynomial is fitted to this portion of the data and subtracted from the measured signal yielding the background corrected signal. In ozone mode, the determination of the order of this polynomial is based on the ratio of the measured signal, minus the background, to the calculated signal, which indicates how fast the noise decays with increasing altitude. In aerosol mode, this determination is based on the correlation between the slope of the logarithm of the background and range corrected signals calculated once from the raw signal and once from the simulated signal. If the background noise is nearly constant with altitude, the order of the polynomial is set to one, if it shows a specific rate of decay, the polynomial order is set to two.

3.1.2. Saturation correction

Below an altitude of around 20 km in ozone mode and 5 km in aerosol mode, the intensity of the backscattered light is sufficiently high that the counting system may become saturated. According to Donovan et al. (1993), the observed counting rate of a paralyzable system can be modeled using a Taylor series as follows:

$$N = S\exp(-\tau_d S)\left[(1-T)+\left(T-\frac{T^2}{2!}\right)\tau_d S + \frac{1}{2!}\left(\frac{T^2}{2!}-\frac{T^3}{3!}\right)(\tau_d S)^2+\cdots\right], \quad (1)$$

where N is the observed counting rate, S is the true counting rate, τ_d is the dead time of the counting system, and T is the discriminator level. Here, Equation (1) is used up to the third order, and the true counting rate S is found with a Newton–Raphson scheme given the observed counting rate N. The dead time τ_d, and the discriminator level T, are parameters of the counting system and are generally known. However, in the case of LOANA, the discriminator level is not directly displayed and needs to be determined by dedicated measurements, which are not performed at regular intervals. Therefore, the value of the discriminator level is derived from comparisons of the retrieved temperature and ozone profiles with the profiles of coincident balloon soundings. The value of the discriminator level is adjusted to optimize the fit of the retrieved profiles with the balloon soundings, but this can only be done when a coincident balloon sounding is available (every one or two months). The saturation correction introduces an important uncertainty into the retrieved profiles, mainly below an altitude of 20 km for ozone and 5 km for aerosol/PSC.

3.1.3. Correction for Rayleigh and Mie extinction, ozone absorption, and range

During its propagation into the atmosphere, the light experiences both Rayleigh and Mie extinction, generated by air molecules and particles with sizes around the incident wavelength (and some multiples), respectively.

Mie extinction is used to retrieve aerosols and PSC properties, but it induces some limitations and

uncertainties to the retrieval of ozone and temperature profiles.

The signal decreases with altitude as z^{-2}. In either mode, ozone or aerosol, the backscattered signal is corrected for range as well as for Rayleigh extinction. For a given altitude z the range and Rayleigh corrected signal, $N'(z)$, is given by

$$N'(z) = N(z) \cdot \exp\left[\left(\sigma(\lambda_e) + \sigma(\lambda_r)\right) \int_0^z n(z')\mathrm{d}z' \right] \cdot z^2, \quad (2)$$

where σ is the Rayleigh extinction cross-section at wavelengths λ_e and λ_r, which refer to the emitted and the received wavelengths, respectively, and $n(z)$ is the air number density. For the Rayleigh channels $\lambda_e = \lambda_r$. It is assumed that this correction does not introduce any statistical error, and hence the relative statistical error of $N'(z)$ is not affected by this correction.

The air number density profile required to calculate the Rayleigh extinction correction is a combination of the MSIS model (Hedin, 1991) and balloon soundings (pressure and temperature), depending on data availability. The Rayleigh extinction cross sections are calculated from the refractive index of air using a standard formula.

The ozone absorption correction is presented in Section 3.3, as only signals used for temperature and aerosol retrieval are corrected for ozone absorption.

3.2. Retrieval of O_3

The DIAL technique is based on the simultaneous recording of two signals at different wavelengths. The first signal, $N_{on}(z)$, is strongly absorbed by ozone, while the second signal, $N_{off}(z)$, is only weakly absorbed. The ozone number density can be derived from these signals as follows:

$$n_{O_3}(z) = \frac{-1}{2(\sigma_{on} - \sigma_{off})} \frac{\mathrm{d}}{\mathrm{d}z} \left(\log \left[\frac{N'_{on}(z) - N_{on,offset}}{N'_{off}(z) - N_{off,offset}} \right] \right), \quad (3)$$

where σ_{on} and σ_{off} are the absorption cross sections at the two wavelengths $\lambda_{on} = 305$ nm and $\lambda_{off} = 355$ nm, respectively, and $N_{on/off,offset}$ are the background terms as described in Section 3.1. The differentiation is performed using a Savitzky-Golay polynomial filter (SG filter) of order 1 (first derivative), and the vertical resolution is defined as the inverse cutoff frequency of the filter, which is given by the maximum frequency that is suppressed by less than 3 dB. The cutoff frequency depends on the number of data points used to calculate one smoothed data point (filter window), and is derived from the transfer function between the unsmoothed derivative and the smoothed derivative, where the former is calculated by a 3 point (non smoothing) SG filter of order 1. This definition is in good agreement with the full width at half maximum of a filtered step function, which is a more intuitive definition of the vertical resolution (see Fig. 3, right panel). The filter window width is increased with altitude to account for the increasing statistical error (noise), as shown in Fig. 3 (left panel).

The relative statistical error of a raw signal is given by Poisson statistics:

$$\Delta N_{on}(z) = \frac{\sqrt{N_{on}(z)}}{N_{on}(z)} \text{ and } \Delta N_{off}(z) = \frac{\sqrt{N_{off}(z)}}{N_{off}(z)}. \quad (4)$$

The logarithm of the ratio and the relative statistical error is given by

$$\hat{N}(z) = \log\left(\frac{N_{on}(z)}{N_{off}(z)}\right), \quad (5)$$

$$\Delta\hat{N}(z) = \frac{1}{\hat{N}(z)} \sqrt{\Delta N_{on}(z)^2 + \Delta N_{off}(z)^2}. \quad (6)$$

And the derivative of the logarithm and the relative statistical error is given by

$$N_{DIAL}(z) = \sum_i c_i \hat{N}(z_i), \quad (7)$$

$$\Delta N_{DIAL}(z) = \frac{1}{N_{DIAL}(z)} \sqrt{\sum_i c_i^2 \Delta\hat{N}(z_i)^2 \hat{N}(z_i)^2}, \quad (8)$$

where c_i are the coefficients of the derivative SG filter. It follows from Equation (3) that the relative statistical error of the ozone profile is:

$$\Delta n_{O_3}(z) = \Delta N_{DIAL}(z). \quad (9)$$

Fig. 4 shows the expected values of the accuracy and statistical error as a function of altitude. Note that both accuracy and statistical error depend to some extent on the conditions under which the measurements were made, and deviate in individual cases from the estimates shown in Fig. 4.

3.3. Retrieval of temperature

Temperature retrieval is performed in several successive steps. First, the 355*H* or 355*M* signal, corrected for background, saturation, range, and Rayleigh extinction (see Section 3.1) is further corrected for ozone absorption. This corrected signal, which is

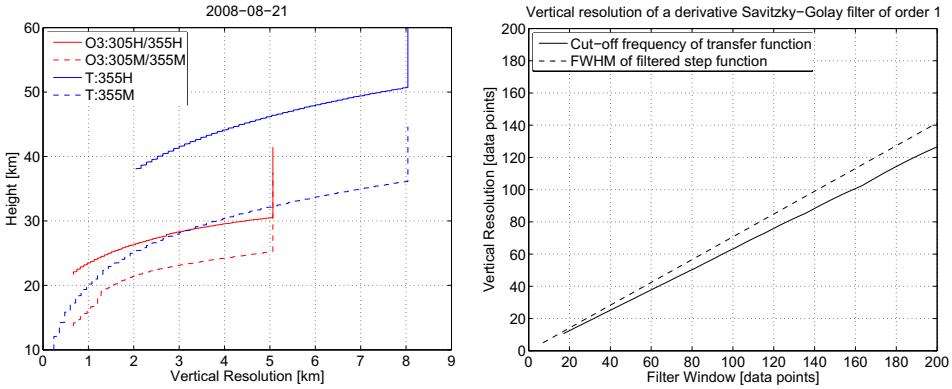

Fig. 3. (Left) Typical vertical resolution of ozone and temperature profiles from the lidar. (Right) Relationship between window width (number of points) and the effective vertical resolution. For comparison, two definitions of the vertical resolution are considered: one based on the cutoff frequency of the filter transfer function, and a second on the filter response to a step function.

proportional to the air number density, is filtered by a digital, non derivative filter and then enters the iterative temperature algorithm.

Let $N(z)$ be the background, saturation, Rayleigh extinction, and range corrected signal divided by the number of laser shots. Then, the signal, corrected for ozone absorption, is given by

$$N'(z) = N(z)\cdot\exp\left[(\sigma(\lambda_e)+\sigma(\lambda_r))\int_0^z n_{O_3}(z')\mathrm{d}z'\right], \quad (10)$$

where $n_{O_3}(z)$ is the number density of ozone at altitude, z and σ are the ozone absorption cross sections at wavelengths λ_e and λ_r, which refer to the emitted and the received wavelengths, respectively. It is again assumed

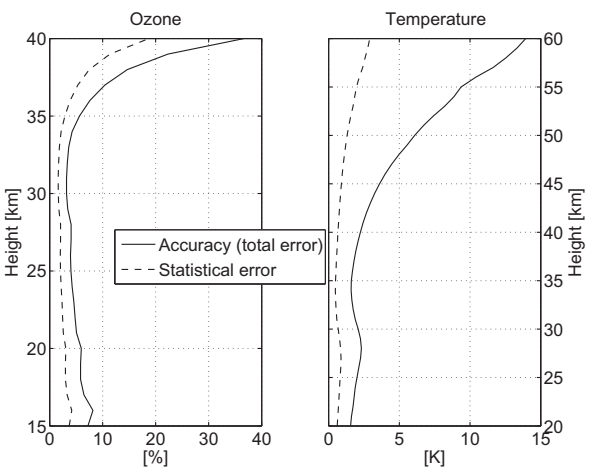

Fig. 4. Average accuracy and statistical error of ozone (left) and temperature (right) for an average integration time of 3.5 h.

that this correction does not introduce any statistical error, and the relative statistical error of $N'(z)$ is given by Equation (4). The corrected signals are filtered by a non-derivative digital filter that generates the smoothed and corrected signals, $N'_{\mathrm{smooth}}(z)$. The vertical resolution (not the filter window), given by the inverse cutoff frequency of the filter, decreases with altitude (see Fig. 3). The relative statistical error of the smoothed signal is given by

$$\Delta N'_{\mathrm{smooth}}(z) = \frac{1}{N'_{\mathrm{smooth}}(z)}\sqrt{\sum_i c_i^2 \Delta N'(z_i)^2 N'(z_i)^2}, \quad (11)$$

where c_i are the coefficients of the digital filter.

The calculation of the temperature profile is based on the discrete forms of the hydrostatic equilibrium equation and on the ideal gas law. Combining these two equations allows us to express $T(z_i)$ as a function of $T(z_{i+1})$:

$$T(z_i) = \frac{\langle N'(z_i, z_{i+1})\rangle Mg}{kN'(z_i)}(z_{i+1}-z_i) + \frac{N'(z_{i+1})}{N'(z_i)}T(z_{i+1}). \quad (12)$$

Here, z_i is the height, M is the mass of an air molecule, g is the gravitational acceleration, k is the Boltzmann factor, and $T(z_i)$ is the temperature at altitude level i. It is evident from this equation that the temperature retrieval process needs to be initialized at some altitude. This process is called tie-on, and occurs at an altitude of around 60 km for the high altitude Rayleigh channel, depending on the quality of the measurements, and at around 40 km for the medium altitude Rayleigh channel. Temperature retrieval by the high Rayleigh channel is initialized by a temperature value taken from MSIS, while initialization of retrieval by the low

channel is based on the temperature derived from the high channel. The absolute error due to the error in the tie-on temperature is given by

$$\Delta T_{\text{tie-on}}(z) = \exp\left[-\frac{Mg}{kT(z)}(z_{\text{tie-on}} - z)\right]\Delta T(z = z_{\text{tie-on}}). \quad (13)$$

As Equation (12) is iterated from top to bottom, the absolute tie-on error decreases exponentially with decreasing altitude. The expected values of accuracy and statistical error are shown in Fig. 4.

3.4. Aerosol and PSC retrieval

The LOANA lidar system operates at the 532 and 1064 nm wavelengths to measure aerosol and PSC backscatter profiles. Aerosols and clouds are characterized according to their optical properties based on classifications that couple the backscatter ratio (R) and the depolarization ratio (δ) as described by David et al. (1998) for single wavelength systems, and by Blum et al. (2005) for multiple wavelength systems.

Measurements are only performed at night and in clear-sky conditions. The acquisition times range from about 30 to 45 min for aerosols, to several hours for PSC. The vertical resolution of the profiles is 60 m, as in ozone mode. To ensure a minimal noise level, lidar signals received on the parallel channel (used for backscatter ratio retrieval) are averaged over intervals of 5 min. Since the SNR is poorer on the perpendicular channel (used for the depolarization calculations), lidar signals on this channel are averaged every 5 min over a moving 15-min interval to keep the same temporal resolution as on the parallel channel. The averaged signals are then inverted using the classical Klett method to derive individual R and δ profiles.

For ozone and temperature retrieval, the aerosol extinction was not taken into account in the inversion procedure. Yet, in the aerosol/PSC retrieval process, the determination of the particle backscatter coefficient (β) requires accurate knowledge of the particle extinction. This correction is central to the Klett inversion procedure we use to retrieve the particle backscattering (Klett, 1981, 1985).

The extinction coefficient $\alpha(z)$ and backscatter coefficient $\beta(z)$ are the sum contributions of both the Mie scattering by particles, $\alpha_p(z)$ and $\beta_p(z)$, and the Rayleigh scattering by molecules, $\alpha_m(z)$ and $\beta_m(z)$; i.e.,

$$\beta(z) = \beta_m(z) + \beta_p(z), \quad (14)$$

$$\alpha(z) = \alpha_m(z) + \alpha_p(z). \quad (15)$$

Scattering by particles is usually characterized by the backscatter ratio R in the parallel plane, defined as unity in the absence of particles ($\beta_p = 0$), and expressed as

$$R(z) = 1 + \frac{\beta_p(z)}{\beta_m(z)}. \quad (16)$$

Characterization of the particle phase is made using the depolarization ratio δ defined as

$$\delta(z) = \frac{R_\perp(z) - 1}{R(z) - 1}\frac{1}{\delta_m}, \quad (17)$$

where $R_\perp(z)$ is the backscatter ratio received in the plane perpendicular to the emitted polarization plane, and δ_m is the molecular depolarization, usually taken to be 0.2%. The calculation of the Rayleigh molecular backscatter coefficient $\beta_m(z)$ and the extinction coefficient $\alpha_m(z)$ is based on absolute atmospheric density profiles derived from local daily meteorological radiosondes.

The determination of the particle backscatter coefficient $\beta_p(z)$ is derived from the simplified lidar equation inversion as

$$P(z) = KP_0\beta(z)\frac{A}{z^2}\exp\left[-2\int_0^z \alpha(z')\mathrm{d}z'\right], \quad (18)$$

where $P(z)$ is the received power from altitude z, P_0 the emitted power, A the surface of the receiving telescope, and K represents the instrumental constants. This inversion relies on the quantitative knowledge of, firstly, the clear-air altitude z_R at which $\beta_p(z_R) = 0$, and then (except when Raman detection is available) of the relationship between $\alpha(z)$ and $\beta(z)$ referred to as the lidar ratio (or phase function) $\varphi(z)$ (Klett, 1981, 1985). If the value of the lidar ratio is assumed to be known, this relationship is

$$\varphi(\lambda, z) = \frac{\alpha(\lambda, z)}{\beta(\lambda, z)}. \quad (19)$$

The main constituents of the atmosphere are assumed to be homogeneous in the 15–35 km range, so the molecular lidar ratio can be regarded as constant with altitude and calculated according to Bodhaine (1999), as follows:

$$\varphi_m(\lambda, z) = \frac{8\pi}{3}. \quad (20)$$

Stratospheric particles can be divided into four classes: background aerosols, volcanic aerosols, PSC, and thin tropopause cirrus. The lidar ratio of these particles can be expressed as

$$\varphi_p(\lambda,z)=\frac{\alpha_p(\lambda,z)}{\beta_p(\lambda,z)}. \quad (21)$$

The background aerosol lidar ratio was calculated from optical aerosol modeling by Rosen and Hofmann (1986) as $\varphi_p = 55$ sr. The volcanic aerosol lidar ratio was estimated following the Pinatubo eruption as $\varphi_p = 40$ sr (Chazette et al., 1995). The PSC and ice clouds lidar ratio is assumed to be $\varphi_p = 18$ sr (Chen et al., 2002; Lampert et al., 2009). We are working on detection of the N_2 Raman scattering associated with the 532 nm wavelength to allow for direct lidar ratio determination. However, without Raman detection, the altitudes of the different particle-type layers have to be identified if we are to determine a lidar ratio profile. A threshold method based on the variance of the range and background-corrected signal is currently used (Chazette et al., 1995). A two step PSC detection method is implemented using an iterative approach with the inverted backscatter profile being used as the control variable instead of the raw background-corrected signal (Gazeaux et al., 2011). The first step performs a statistical stationarization of typical background profiles (with a non-constant trend and altitude increasing variability). The second step performs a statistical test based on the likelihood of maximization. Finally, β and R are calculated from the standard Klett formulas. To a large extent, the intensity of the detected signals is determined by the laser power, among which the N_2-scattered vibrational Raman detected signal is always the weakest. In the LOANA system, this power is currently too low for the inversion process to use the 607 nm Raman signal scattered from the 532 nm wavelength as a way to derive a particular extinction at stratospheric altitudes. Uncertainties in β and R are derived from long-term statistical analysis (Chazette et al., 1995; David et al., 1998). Signal fluctuations due to random detection processes induce errors of about 5% in R. The reference altitude used in the Klett inversion (or the presence of particles at this given altitude) leads to uncertainties of between 5% and 10% in R. The lidar ratio and its altitude dependence cause uncertainties of around 20% in R. Therefore, the total resulting uncertainty in R up to 35 km, and for a minimum time integration of 30 min, lies between 5% and 10%. For wavelengths shorter than 532 nm, the lidar ratio remains the critical parameter. Above the 800 nm range, the clear-air altitude drives the overall uncertainty in the inversion procedure (Ansmann et al., 1992).

On the perpendicular channel, the signal becomes very noisy above 25–30 km, and this results in a large uncertainty in the a priori knowledge of the backscatter. For a given uncertainty of 7% on the parallel channel, and a 20% uncertainty on the perpendicular channel, the total error in the depolarization ratio is about 25% to 30% (David et al., 1998).

4. Validation

4.1. Reference instruments

4.1.1. Balloon soundings

Daily meteorological radiosoundings are conducted at DDU by the French Meteorological Institute (Météo-France), with profiles dating back to 1957. These meteorological observations at altitude are made within the intergovernmental agreement coordinated by WMO to ensure optimum horizontal sampling in this region, where observational coverage is poor. Measurements are performed daily at 00:00 UT using standard meteorological sensors carried by balloon, and include pressure, temperature, and humidity detection (PTU). Data are transmitted in real time to the ground station.

Ozone soundings (by balloon) are carried out at DDU monthly, with additional soundings during the ozone hole season, from October to January. PTU measurements have also been made, together with the ozone soundings, since 1992, but with a lower frequency than the daily Météo-France soundings. Approximately 30 PTU soundings per year are performed using ozone balloons, with a higher launch frequency during the austral summer. Electrochemical Concentration Cell (ECC) ozone sondes provide ozone profiles from the ground up to the burst altitude, which is typically between 25 and 30 km. The measurement uncertainty is about 5% in the stratosphere up to 10 hPa, and from 5% to 25% between 10 and 3 hPa (Jiang et al., 2007, and references therein). Correlative ECC ozone profiles are measured within ±24 h from the center of the lidar integration time interval. For the comparison, the ECC profiles are interpolated to the altitude grid of the lidar, but no smoothing is applied. A total of 39 profile pairs are available from 2008 to 2009. Two comparisons between ECC and lidar are shown in Fig. 5. They demonstrate the ability of the lidar system to resolve vertical structures with scales of 1 km in the lower and middle stratosphere.

4.1.2. Aura/MLS

Microwave Limb Sounder (MLS) ozone and temperature profiles have been extensively validated [e.g. Jiang et al., 2007; Froidevaux et al., 2008; Schwartz et al., 2008]. The key characteristics of

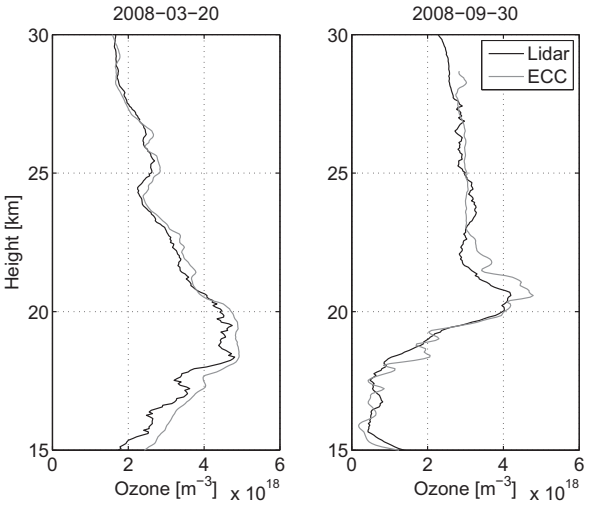

Fig. 5. Single profiles of ozone measured by the lidar (black) and by the balloon sounding (gray) on 20 March 2008 (left) and 30 September 2008 (right). The integration period was approximately 4 h for both lidar profiles.

these products are indicated in Table 1. Due to the limited influence of the a priori profile on MLS retrieval, and because of the good vertical resolution, the use of the averaging kernels in this validation study would have had only a minor influence; consequently, we decided not to apply them. For the comparison, we only used nighttime MLS profiles that fulfilled the following criterion: $\Delta t < 24$ h, $\Delta x < 500$ km, and $\Delta y < 100$ km, where t is time, x longitudinal distance, and y latitudinal distance (corresponding to $\Delta\text{lon} < 11^\circ$ and $\Delta\text{lat} < 0.9^\circ$ at 66.4°S). The MLS data were screened according to the recommendations in the data user guide of version 2.2 (Livesey et al., 2007). A total of 162 profile pairs are available for the intercomparison.

4.1.3. TIMED/SABER

The Sounding of the Atmosphere using Broadband Emission Radiometry (SABER) experiment is dedicated to exploring the thermal structure and energetics of the middle and upper atmosphere, and concentrates mainly the upper mesosphere and lower thermosphere. It provides profiles of temperature and trace gases in an altitude domain ranging from 100 to 0.0001 hPa (16–100 km). However, in this study, we use only temperature in the comparisons (version 1.07). The reported precision at 10 hPa (1 hPa) is better than 0.5 K (1 K), and the accuracy better than 1 K (2 K) (Remsberg et al., 2008). The same coincidence criteria have been applied as for the MLS data (see Section 4.1).

Table 1
Key characteristics of the MLS ozone and temperature standard products (Froidevaux et al., 2008; Schwartz et al., 2008).

	Mid. strat. (10 hPa)	Upper strat. (1 hPa)
Ozone		
Accuracy	<10%	<10%
Precision	5%	10%
Vertical resolution	3 km	3 km
Horizontal resolution	300 km	300 km
Temperature		
Accuracy	2 K	2.5 K
Precision	1 K	2 K
Vertical Resolution	4 km	8 km
Horizontal Resolution	165 km	165 km

4.1.4. CALIOP

The Cloud-Aerosol LIdar with Orthogonal Polarization (CALIOP) operates onboard the Cloud-Aerosol Lidar and Infrared Pathfinder Satellite Observations (CALIPSO) spacecraft, which is in a sun-synchronous orbit that crosses the equator southward at 01:50, and northward at 13:50, local standard time (Winker et al., 2009). The CALIPSO satellite was launched in April 2006 and follows the same track every 16 days (Currey et al., 2007). CALIOP Level 1 Lidar 532-nm total attenuated backscatter data are used in this study (Currey et al., 2007). Selected overpasses near reference ground-based lidar stations were used. To compare cloud structure and optical depth derived from CALIOP and ground-based lidar, we applied an optimal temporal and spatial collocation routine that transforms ground time series into latitude–longitude trajectories based on vertical wind profiles. Cloud base and top height are obtained using a wavelet analysis (Morille et al., 2007). Cloud optical depths are retrieved for cloud layers using a standard transmission-loss algorithm (e.g., Platt, 1973). This algorithm derives the attenuation produced by a given cloud layer, and hence its optical depth, by comparing the molecular backscatter in the free troposphere above and below the layer. Forward scattering effects are accounted for by parameterization (Chen et al., 2002).

4.2. Ozone

Fig. 6 (left) shows the profile of the mean relative difference between lidar and ECC. Particularly good agreement is found between 25 and 34 km, where little or no bias can be identified, with the differences here being less than 2%. Between 17 and 25 km, the lidar is biased low by −3% on average with respect to the ECC. Time series of the differences in ozone at 15, 20,

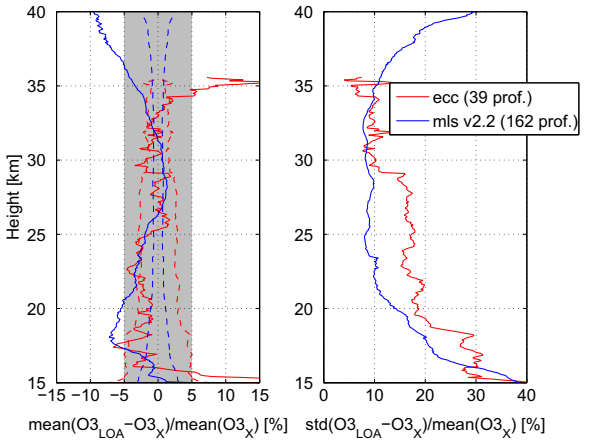

Fig. 6. (Left) Profiles of mean ozone differences between the lidar (average integration time of 3.5 h) and the reference instruments: ECC (red) and MLS (blue). The dashed lines represent the error associated with the mean ($\sigma N^{-1/2}$). (Right) Standard deviation of the differences between data from the lidar and reference instruments. (For interpretation of the references to colour in this figure legend, the reader is referred to the web version of this article.)

and 27 km give an insight into the stability of the lidar system (see Fig. 7). While the scatter of the residuals is slightly larger in 2009 than in 2008, no significant change is visible in the mean value.

Fig. 6 (left) shows the profile of the mean difference in ozone between the lidar and the MLS. The lidar develops a low bias with respect to MLS below 25 km, reaching −8% at 18 km. Between 25 and 33 km, the two instruments agree within ±2%, while above 33 km the lidar is again biased low with respect to the MLS (−10% at 40 km). Comparisons between the MLS data and ozone sondes at four Antarctic stations reveal a similar structure, with the MLS being generally higher around 10 and 100 hPa, but lower around 30 hPa (Jiang et al., 2007). With differences of less than 10% between 15 and 40 km compared with the MLS, the performance of the LOANA lidar system is comparable to the performances of older, well characterized systems such as the lidar operating at the Observatoire de Haute-Provence (France), Mauna Loa (Hawaii), or Table Mountain (California) (Jiang et al., 2007).

In the bottom panel of Fig. 8 time series of the differences between the lidar and MLS ozone measurements are shown for three different altitudes. While the bias is constant, the scatter of the difference between the lidar and MLS measurements at 40 km increased from 2008 to 2009.

4.3. Temperature

The daily Météo-France balloon payloads are equipped with MODEM PTU sensors (M2K2) to measure temperature, pressure, and relative humidity.

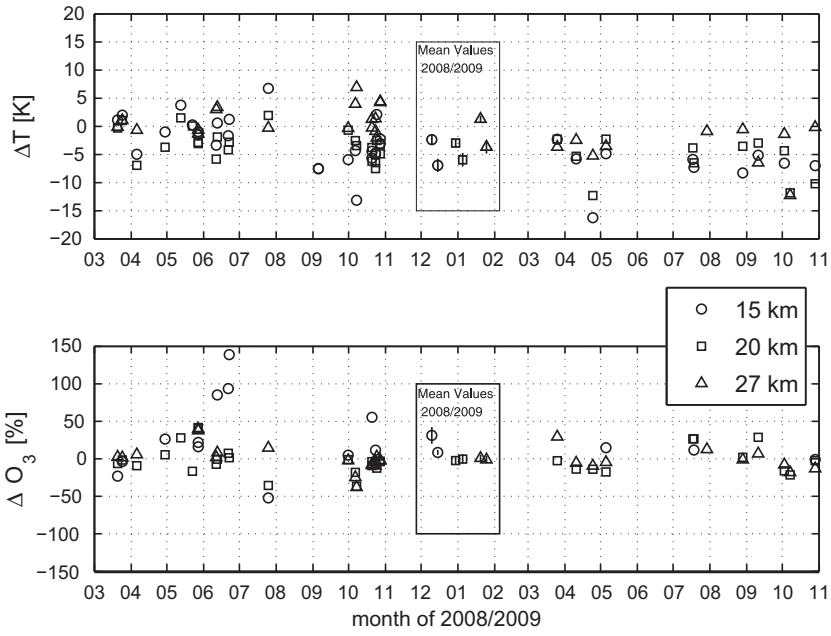

Fig. 7. Time series of differences in temperature (top) and ozone (bottom) between lidar and balloon data (PTU and ECC for temperature and ozone, respectively) at three different altitudes. The frame highlights the mean values for 2008 (left) and 2009 (right). Error bars indicate the error associated with the mean values ($\sigma N^{-1/2}$).

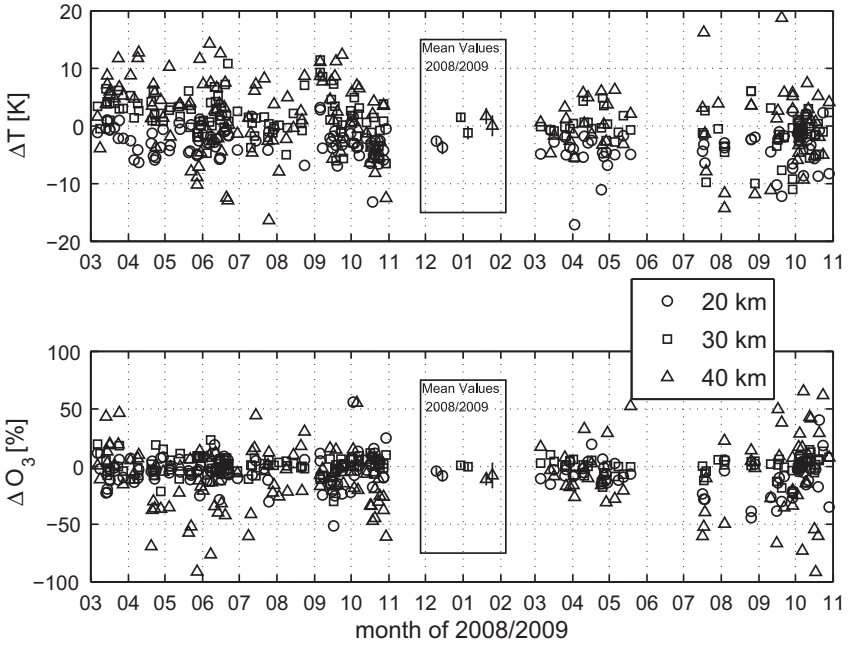

Fig. 8. Time series of differences in temperature (top) and ozone (bottom) between lidar and MLS data at three different altitudes. The frame highlights the mean values for 2008 (left) and 2009 (right). Error bars indicate the error associated with the mean values ($\sigma N^{-1/2}$).

The same sensors are used on the ozone balloon payload. Two examples of individual temperature profiles are shown in Fig. 9. The difference profiles (Fig. 10), reveal a distinct cold bias below 23 km, of up to −4 K at 20 km. A small cold bias of less than −1 K is found between 23 and 32 km. Above this, a large discrepancy between the lidar and sonde measurements is observed that might be attributed to the rather poor performance of the PTU sensors at these altitudes. Time series of differences between MODEM PTU sensors and lidar, shown in the top panel of Fig. 7, reveal a larger cold bias in 2009 than in 2008. At 27 km, a bias of −4 K occurred 2009, while in 2008 the lidar was 1 K warmer than the PTU soundings.

The profile of mean differences in temperature between the MLS and lidar measurements is shown in Fig. 10. This behavior is consistent with that observed in the comparison with the radiosondes: the lidar temperature measurements show a low bias below 27 km, with a maximum bias of −3 K at 20 km. Between 30 and 40 km, the agreement is good. However, the lidar is warmer than the MLS by 1 K. At 47 km, a negative peak (−2.2 K) in the difference profile is observed. It should be noted that the MLS tends to be biased warm at this altitude (Schwartz et al., 2008).

Time series of the differences in temperature are shown in Fig. 8. In 2009, the lidar temperatures are generally lower than the MLS temperatures, but this difference is statistically significant only at 30 km. Vertical profiles of the mean differences between SABER and lidar are shown in Fig. 10 revealing a cold bias below 30 km that increases up to −6 K at 20 km. This cold bias, which is larger than that associated with the MLS by a factor of 2 (and larger than that associated with MODEM by a factor of 1.5), might be partly due to the SABER temperature readings being too warm below 40 km (Remsberg et al., 2008). Between 30 and 45 km, the agreement with SABER is better than 1 K. At 50 km, a peak of 4 K is found in the difference profile.

Fig. 11 shows time series of the differences between LOANA and SABER. Temperatures are systematically lower in 2009 than in 2008; however, at 40 and 50 km, the differences are not statistically significant.

4.4. Diurnal variations in temperature

Diurnal variations in temperature due to atmospheric tides can introduce bias when comparing instruments that sample systematically at different times. Consequently, it is important to characterize such variations and to study their effect on the validation. To our knowledge, no previous observations of tidal temperature signatures in the Antarctic stratosphere have been made.

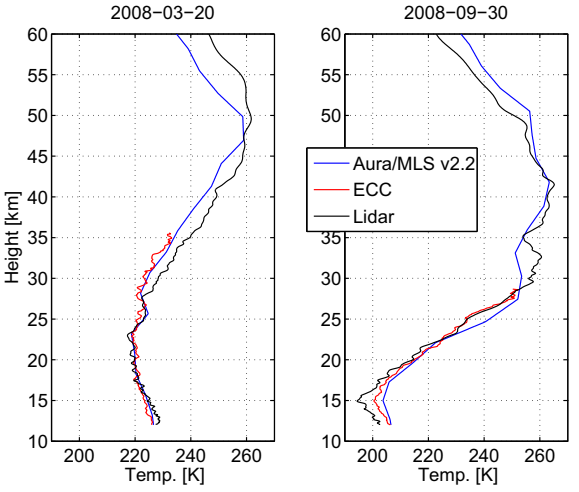

Fig. 9. Single profiles of temperature on 20 March 2008 (left) and 30 September 2008 (right) measured by the lidar (black), balloon sounding (red), and satellite (blue). The integration period was approximately 4 h for both lidar profiles. (For interpretation of the references to colour in this figure legend, the reader is referred to the web version of this article.)

In July 2008, during the Antarctic polar night, the lidar operated almost daily in aerosol mode. In this mode, temperature is derived from the 532 nm signal, instead of the 355 nm signal as in ozone mode. The same algorithm presented in Section 3 is used for these retrievals. However, a linear background fit was applied in each case, and no saturation correction made. Thus, the profiles cover the altitude range from 30 to 60 km. The temperature profiles compare well with those derived from the 355 nm channel as shown in Fig. 12. The temperature datasets measured in aerosol mode from 2008 to 2009 have been compared with the MLS and SABER data revealing an average bias of −2 K between 30 and 50 km with respect to MLS and SABER (see Fig. 13). In contrast, the standard deviation of the differences is somewhat smaller than those found for temperature data retrieved at 355 nm. Figs. 13 and 10 reveal a systematic difference between the temperature derived from the ozone and aerosol modes this needs further investigation.

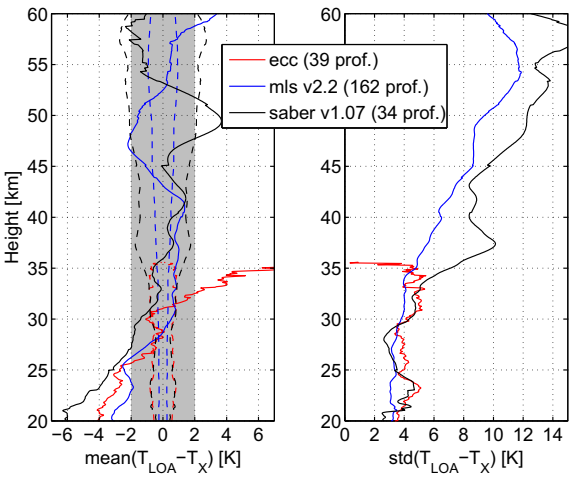

Fig. 10. (Left) Profiles of mean differences between lidar data (average integration time of 3.5 h) and the reference instruments: PTU coupled with ECC (red), MLS (blue), and SABER (black). The dashed lines in the left panel represent the error associated with the mean values ($\sigma N^{-1/2}$). (Right) Standard deviation of the differences. (For interpretation of the references to colour in this figure legend, the reader is referred to the web version of this article.)

To investigate diurnal variations, signals were integrated over 1 h to derive the temperature profiles. In the next step, the hourly anomalies, $\Delta T(z,t)$, ere calculated from the difference between the profiles derived from the 1-h integrations and the profiles derived from the one-day integration. Because of the noisy nature of the hourly anomalies, they were further averaged over all days yielding the mean hourly anomalies for the entire month. The mean hourly anomalies have again been averaged over a time window from 00:00 to 15:00 and 15:00 to 24:00 UT. These two data vectors are an estimate of the mean deviation from the daily mean temperature at 10:00 and 19:00 (see Fig. 14) and do not allow us to derive a complete characterization of the temperature tides. Fig. 14 shows the observational results from a height of 48 km, together with the diurnal cycle as simulated by the LMDz (Laboratoire de Météorologie Dynamique) climate model (Eyring et al., 2006, and references therein), and reveals reasonable agreement between data from the model and observations. Based on these data, the amplitude of the diurnal temperature tide at DDU at 48 km is estimated to be around 1 K. In Fig. 15 the annual cycle of the amplitude and phase of the diurnal tide derived from LMDz simulations above DDU at a height of 48 km is compared with the results of the Global Scale Wave Model (GSWM-00, Hagan and Forbes, 2002), hereafter referred to as GSWM) at a latitude of 66°S. Both models show minimum amplitudes in June. However, for months 5–8 and 10, the LMDz amplitudes are larger by a factor of 2 compared with those from the GSWM.

As 98% of both the lidar and MLS profiles are sampled between 10:00 and 20:00 UT, which corresponds approximately to the positive phase of the diurnal cycle, and as the amplitudes are expected to be less than 1.5 K throughout the year, the cold bias at 48 km with respect to the MLS is unlikely to be due to

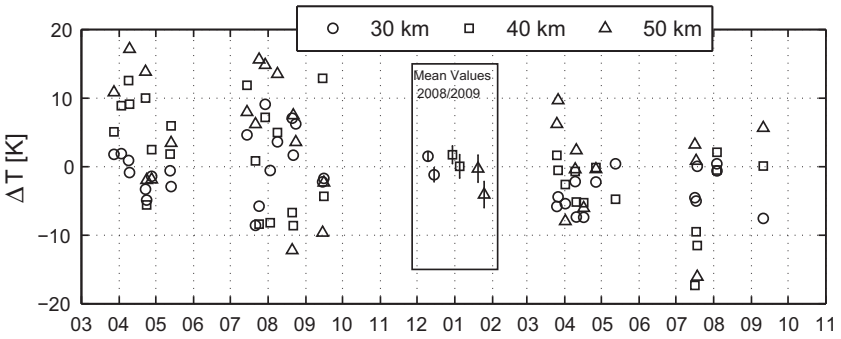

Fig. 11. Time series of differences in temperature between lidar and SABER at three different altitudes. The frame highlights the mean values for 2008 (left) and 2009 (right). The error bars indicate the error associated with the mean values ($\sigma N^{-1/2}$).

tidal effects. 70% of the SABER profiles are sampled between 10:00 and 20:00 UT, and the remaining 30% are almost equally distributed over the rest of the day. Thus, tides are not likely to explain the warm bias of 2–4 K at 48–50 km.

4.5. Polar stratospheric clouds and aerosols

The atmospheric community now has access to an ensemble of dedicated satellite observations (ENVISAT, ODIN, CALIPSO, and the upcoming EarthCARE and Adm-AEOLUS) that present the significant possibility of solving most of the divergences between models and observations. While ground-based measurements are used to validate satellite observations, such measurements are also coupled with satellite data. In this context, we compared data acquired using the LOANA system with measurements made by the CALIOP lidar on board CALIPSO (which follows a sun-synchronous orbit with a 16-day track overpass). The CALIPSO trajectories above DDU are typically almost perpendicular to the trajectories of the air masses; consequently, co-location is never fully achieved. In addition, ground-based measurements are weather dependent (needing clear-sky conditions), whereas the satellite delivers continuous measurements. It appears that the temporal and horizontal variability remain large, and if coincidences are not achieved within a typical window of 10 km and 1 h, quantitative comparison is not possible due to both measurement variability at the edge of the vortex in winter, and the expected noise in a narrow time integration window. To compare CALIOP with ground-based lidar observations, an optimal temporal and

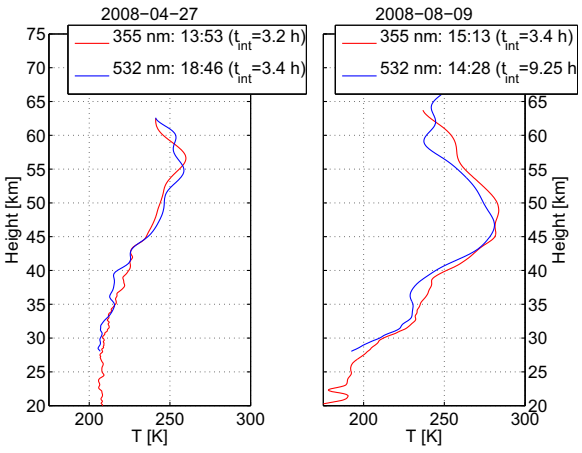

Fig. 12. Examples of temperature profiles retrieved from the channel at 355 nm, in ozone mode (red) and at 532 nm in aerosol mode (blue). (For interpretation of the references to colour in this figure legend, the reader is referred to the web version of this article.)

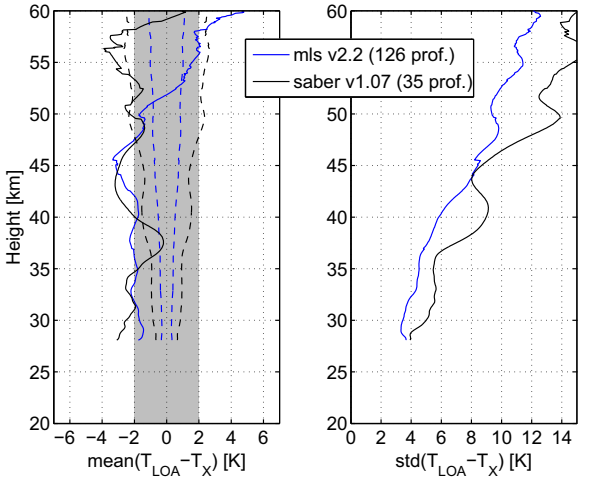

Fig. 13. Profiles of mean (left) and standard deviation (right) of the temperature differences between the lidar (in aerosol mode) and MLS (blue), and the lidar and SABER (black) data. (For interpretation of the references to colour in this figure legend, the reader is referred to the web version of this article.)

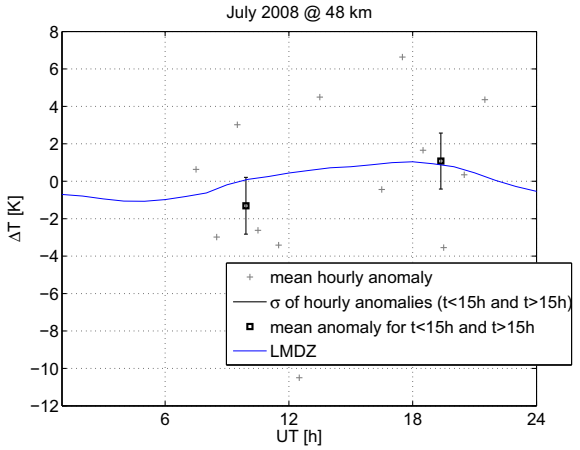

Fig. 14. Modeling and observation of the diurnal cycle of temperature over Dumont d'Urville at 48 km in July 2008. The crosses represent the hourly deviations from the daily retrieval averaged over all available days of the month. The squares and their error bars are the means and standard deviations of the hourly deviations before and after 15:00 UT. The blue solid line represents the diurnal cycle derived from hourly output of the LMDz model. (For interpretation of the references to colour in this figure legend, the reader is referred to the web version of this article.)

spatial co-location is found by estimating the latitude–longitude trajectory of the atmospheric column observed from the ground. This trajectory is estimated by calculating the vertical profile of wind speed and direction above the site from local daily radiosonde profiles or from NCEP data. Hence, we obtain two trajectories, one from CALIOP and the other from the ground, which can be compared. If the trajectories are perpendicular, the attenuated backscatter profiles and cloud properties will be compared at the intersection of the two trajectories rather than at the site overpass time. If the two trajectories are not perpendicular, their intersection will be too far away, and the comparison is then performed at the time and location of the closest ground site overpass.

Fig. 16 shows the CALIOP total attenuated backscatter profiles from an orbit passing over a position close to DDU, and a time series of the DDU lidar total attenuated backscatter for a time period near the CALIOP overpass on 3 July 2007. The 6-h DDU lidar time series was converted into a latitude–longitude trajectory using NCEP wind profiles. The intersection between the two trajectories was about 150 km east of DDU station at 14:58 UTC. Fig. 17 shows the CALIOP and DDU lidar total attenuated backscatter profiles (532 nm) at the trajectory intersection. Both profiles reveal significant attenuation from a tropospheric cloud ranging from 6500 to 12,000 m altitude, and a stratospheric cloud ranging from 14,000 to 19,000 m altitude. The optical depths derived from the DDU lidar were 0.56 and 0.26 for the tropospheric and stratospheric clouds, respectively. Values of the optical

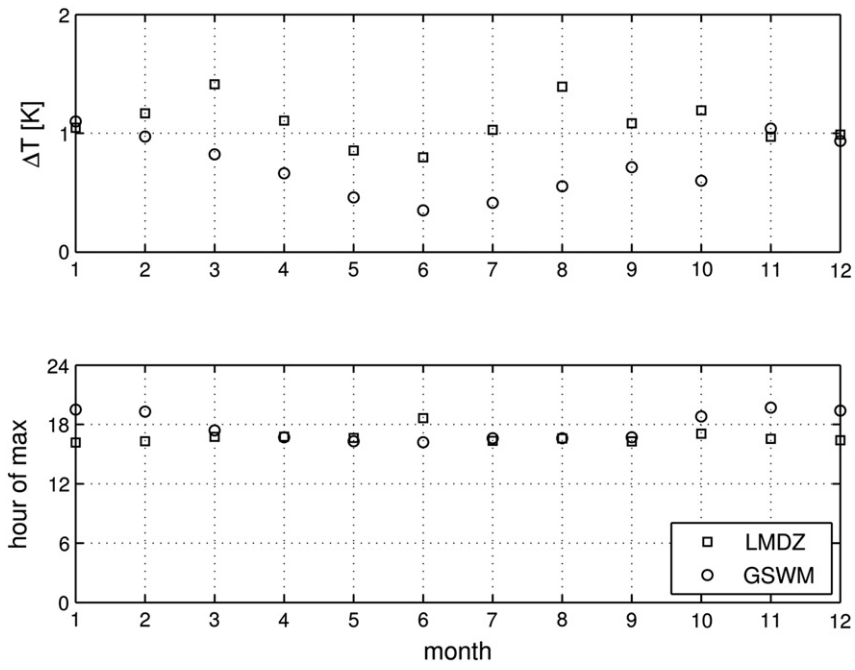

Fig. 15. Amplitude (top) and phase (bottom) of the diurnal temperature tide at 48 km as modeled by LMDz and the Global Scale Wave Model (GSWM) at DDU (66°40′S, 140°01′E).

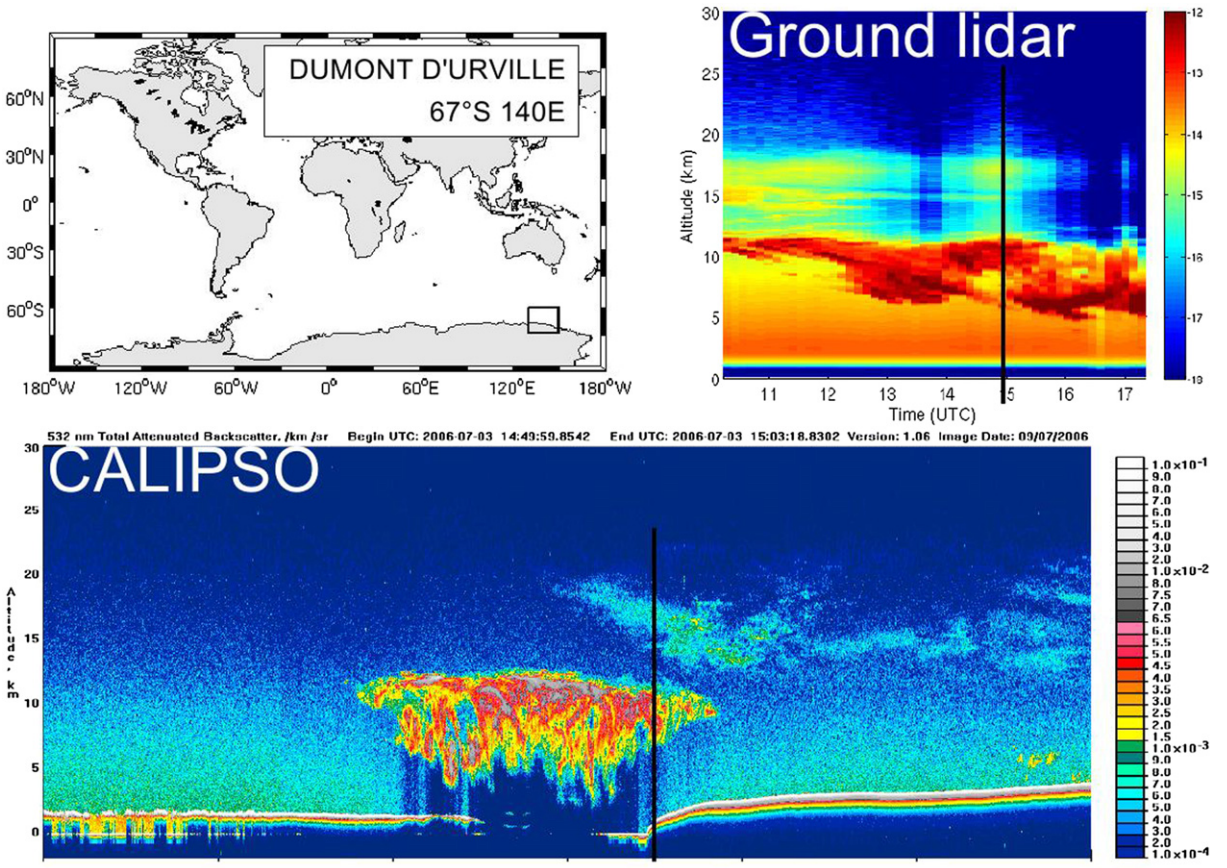

Fig. 16. Height–time cross sections of total attenuated backscatter measured by the ground-based lidar LOANA (top right) and by the spaceborne CALIOP instrument (bottom panel). The intersection between the two cross sections is marked with a black line. The top left panel indicates the region of CALIOP measurements, centered on DDU.

depth retrieved from CALIOP data were about 30% lower.

5. Discussion

Ozone and temperature data obtained from the Lidar Ozone and Aerosol for NDACC in Antarctica (LOANA) at Dumont d'Urville, Antarctica, have been compared with correlative ozone and temperature profiles from balloon soundings (classical PTU and ozone soundings), and from MLS and SABER (only temperature). The ozone comparisons reveal good agreement between the lidar and the other data sources, with mean differences lower than 5% between 20 and 35 km. At higher altitudes, the bias compared with MLS increases to −10% at 40 km. The differences between the lidar and balloon data, and between the lidar and MLS data, were essentially the same in 2008 and in 2009, showing a high stability of the lidar ozone measurements.

For temperature, the comparison revealed an agreement with the reference instruments of within 2 K between 27 and 47 km, and of less than 4 K between 25 and 60 km. Below 30 km, a large bias was observed with the same sign, suggesting a systematic offset of the lidar measurements, which could be caused by aerosol scattering interferences. With respect to both MLS and SABER, we found somewhat larger differences in the stratopause region, but with the opposite sign. Consequently, it is not clear whether this can be attributed to the lidar or to the satellite measurements. We attempted to derive tidal signatures from the lidar temperature data (at 532 nm) at a height of 48 km, and compared the results with calculations of the LMDz and GSWM models. The emerging picture is very consistent, indicating that the diurnal tide has a maximum at 18:00 UT, with an amplitude of around 1 K in July. According to the models, the amplitude has a minimum in June of around 0.5–1 K, and two maxima of 1–1.5 K around the equinox. Based on

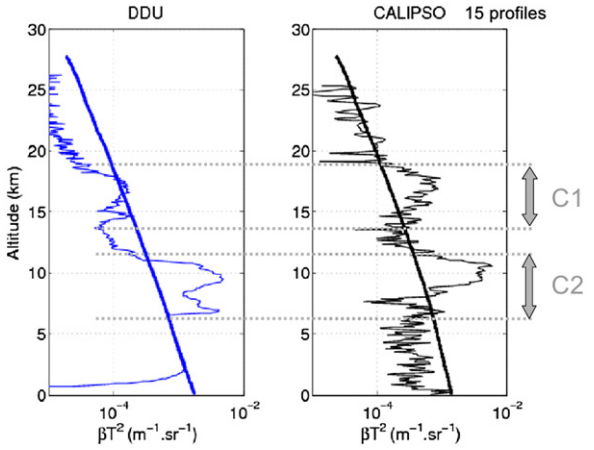

Fig. 17. Comparison of backscatter lidar signals observed from CALIPSO and DDU at the intersection point (150 km east of DDU on 3 July 2007), taking into account Lagrangian air mass transport.

these results, and on the analysis of the time sampling of the different instruments, tidal effects cannot explain the biases found in the stratopause region.

Compared with balloon measurements, SABER, and to some extent to MLS, there is a drop in the temperature bias between 2008 and 2009 at altitudes below 30 km. At 40 and 50 km, the change in bias is still present, but not statistically significant. We assume that there was a change in lidar temperatures, but cannot suggest a likely explanation for this. Note that maintenance is only performed once a year, during the austral summer, followed by a short period of testing before the system runs with minimal modifications for the rest of the year. This approach may introduce some interannual variability related to instrument performance.

Backscatter profiles were compared with CALIOP measurements using a Lagrangian approach to achieve the best match between the two instruments. Agreement in terms of attenuated backscatter and in terms of derived optical depth was good. Other approaches have used Lagrangian modeling to improve the spatio-temporal coincidences. These case studies, which couple microphysical modeling and lidar measurements, reveal that the relative accuracy of the temperature fields required for global modeling is critical, and often hinders PSC formation as it is a sensitive threshold formation process; a 1 K temperature uncertainty being, in most cases, too large to be considered adequate (Jumelet et al., 2009).

To some extent, these issues could be addressed with CALIOP optical properties assimilation. However, this approach would require detailed aerosol and cloud microphysics to be able to accurately simulate the optical properties of the particles. Consequently, it would also require an extensive size-resolved particle scheme to be implemented in high-resolution advection models. The latter remains difficult to implement at the global scale. Future work on assimilation will be performed based on a first successful modeling of different volcanic aerosol plumes using CALIOP data assimilation in the global high resolution microphysical transport MIMOSA model (Jumelet et al., 2009).

At the instrumental level, additional wavelengths and N_2 vibrational Raman detection are planned for a forthcoming major design update: this will avoid saturation effects and so improve data quality in the lower stratosphere, as well as improving the particle characterization. Extended detection capabilities will allow for microphysical parameter retrieval (e.g., particle size or type). This can provide additional constraints to the models, and help to improve PSC modeling.

Based on this, and other intercomparison studies of stratospheric ozone and temperature that included lidars, we conclude that the performance of this instrument compares well with other lidar systems. The LOANA instrument is the only lidar that has provided continuous measurements of aerosols and PSC for the last two decades (since 1989) on the Antarctic continent, and the only one measuring ozone. Since 2006, it has also been able to derive stratospheric temperature profiles.

The evolution of the stratosphere has been recognized as an essential component of changes to stratospheric ozone levels, and also of climate change. The LOANA observations have recently contributed to identifying and monitoring these changes in stratospheric temperatures over DDU, and the potential correlative impact on PSC formation frequency (David et al., 2010). Both the continuity and adequacy of the observations underline the importance of such an instrument in Antarctica within NDACC.

References

Adriani, A., Massoli, P., Donfrancesco, G.D., Cairo, F., Moriconi, M.L., Snels, M., 2004. Climatology of polar stratospheric clouds based on lidar observations from 1993 to 2001 over McMurdo Station, Antarctica. J. Geophys. Res. 109

Ansmann, A., Wandinger, U., Riebesell, M., Weitkamp, C., Michaelis, W., 1992. Independent measurement of extinction and backscatter profiles in cirrus clouds by using a combined Raman elastic-backscatter lidar. Appl. Opt. 31, 7113–7131.

Blum, U., Fricke, K., Mller, K., Siebert, J., Baumgarten, G., 2005. Long-term lidar observations of polar stratospheric clouds at Esrange in northern Sweden. Tellus 57B, 412–422.

Bodhaine, B., 1999. On Rayleigh optical depth calculations. Am. Meteorol. Soc. 16, 1854−1861.

Chazette, P., David, C., Lefrère, J., Pelon, J., Godin, S., Mgie, G., 1995. Study of the optical, geometrical and dynamical properties of stratospheric post-volcanic aerosols from lidar remote sensing at 532 nm, following the eruptions of El Chichon and Mt Pinatubo. J. Geophys. Res. 100, 23195−23207.

Chen, W.N., Chiang, C.W., Nee, J.B., 2002. Lidar ratio and depolarization ratio for cirrus clouds. Appl. Opt. 31, 6470−6476.

Currey, J., et al., 2007. Cloud Aerosol Lidar Infrared Pathfinder Satellite Observations. Data Management System, Data Products Catalog. Document No: PC-SCI-503.

David, C., Bekki, S., Godin, S., Mégie, G., Chipperfield, M., 1998. Polar stratospheric clouds climatology over Dumont d'Urville between 1989 and 1993 and the influence of volcanic aerosols on their formation. J. Geophys. Res. 103, 22163−22180.

David, C., Bekki, S., Berdunov, N., Marchand, M., Snels, M., Mégie, G., 2005. Classification and scales of Antarctic polar stratospheric clouds using wavelet decomposition. J. Atmos. Solar-Terrestr. Phys. 67, 293−300.

David, C., Keckhut, P., Armetta, A., Jumelet, J., Marchand, M., Bekki, S., 2010. Radiosonde stratospheric temperatures at Dumont d'Urville (Antarctica): trends and link with polar stratospheric clouds. Atmos. Chem. Phys. 10, 3813−3825.

Donovan, D.P., Zhiteway, J.A., Carswell, A.I., 1993. Correction for nonlinear photon-counting effects in lidar systems. Appl. Opt. 32, 6742−6753.

Eyring, V., et al., 2006. Assessment of temperature, trace species and ozone in chemistry-climate model simulations of the recent past. J. Geophys. Res. 111

Froidevaux, L., et al., 2008. Validation of Aura Microwave Limb Sounder stratospheric ozone measurements. J. Geophys. Res. 113, D15S20.

Gazeaux, J., Bekki, S., Naveau, P., Keckhut, P., Jumelet, J., Paredes, J., David, C., 2011. Detection of particles layers in backscatter profiles: application to Antarctic lidar measurements. Atmos. Chem. Phys. Discuss. 11, 21935−21969.

Hagan, M.E., Forbes, J.M., 2002. Migrating and nonmigrating diurnal tides in the middle and upper atmosphere excited by tropospheric latent heat release. J. Geophys. Res. 107

Hedin, A., 1991. Extension of the MSIS thermosphere model into the middle and lower atmosphere. J. Geophys. Res. 96, 1159−1172.

Jiang, Y.B., et al., 2007. Validation of Aura Microwave Limb Sounder ozone by ozonesonde and lidar measurements. J. Geophys. Res. 112

Jumelet, J., Bekki, S., Seifert, P., Montoux, N., Vernier, J., Pelon, J., 2009. Microphysical modelling of a mid-latitude, polar stratospheric cloud event: comparisons against multiwavelength ground-based and spaceborne lidar data. J. Geophys. Res.

Klett, J., 1981. Stable analytical inversion solution for processing lidar returns. Appl. Opt. 20

Klett, J., 1985. Lidar inversion with variable backscatter/extinction ratios. Appl. Opt. 24, 1638.

Lampert, A., Ehrlich, A., Dörnbrack, A., Jourdan, O., Gayet, J., Mioche, G., Shcherbakov, V., Ritter, C., Wendisch, M., 2009. Microphysical and radiative characterization of a subvisible midlevel Arctic ice cloud by airborne observations − a case study. Atmos. Chem. Phys. 9, 2647−2661.

Livesey, N.J., et al., 2007. Version 2.2 Level 2 Data Quality and Description Document. Technical Report. Jet Propulsion Laboratory, California Institute of Technology, Pasadena.

Morille, Y., Haeffelin, M., Drobinski, P., Pelon, J., 2007. An automated algorithm to retrieve the vertical structure of the atmosphere from single-channel lidar data. J. Atmos. Ocean. Technol. 24, 761−775.

Platt, C.M.R., 1973. Lidar and radiometric observations of cirrus clouds. J. Atmos. Sci. 30, 1191−1204.

Remsberg, E.E., et al., 2008. Assessment of the quality of the Version 1.07 temperature-versus-pressure profiles of the middle atmosphere from TIMED/SABER. J. Geophys. Res. 113, D17101.

Rosen, J., Hofmann, D., 1986. Optical modelling of stratospheric aerosols: present status. Appl. Opt. 25, 410−419.

Sacco, V.M., Castagnoli, F., Morandi, M., Stefanutti, L., 1989. Elastic backscattering lidar system for atmospheric measurements in Antarctica. Opt. Quant. Electr. 21, 215−226.

Santacesaria, V., MacKenzie, A., Stefanutti, L., 2001. A climatological study of polar stratospheric clouds (1989−1997) from lidar measurements over Dumont d'Urville (Antarctica). Tellus (B) 53, 306−321.

Schwartz, M.J., et al., 2008. Validation of the Aura Microwave Limb Sounder temperature and geopotential height measurements. J. Geophys. Res. 113

Stefanutti, L., Castagnoli, F., Guasta, M.D., Morandi, M., Sacco, V., Zuccagnoli, L., Godin, S., Mégie, G., Porteneuve, J., 1992. The Antarctic ozone lidar system. Appl. Phys. 55, 3−12.

Winker, D.M., Vaughan, M.A., Omar, A.H., Hu, Y., Powell, K.A., Liu, Z., Hunt, W.H., Young, S.A., 2009. Overview of the CALIPSO mission and CALIOP data processing algorithms. J. Atmos. Ocean. Technol 26, 2310−2323.